

The interaction between viscous fingering and wrinkling in elastic-walled Hele-Shaw cells

D. Pihler-Puzović, A. Juel and M. Heil¹

*Manchester Centre for Nonlinear Dynamics and School of Mathematics,
University of Manchester, Oxford Road, Manchester M13 9PL,
United Kingdom*

The development of viscous fingers in circular Hele-Shaw cells is a classical and widely-studied fluid mechanical problem. The introduction of wall elasticity (via the replacement of one of the bounding plates by an elastic membrane) can weaken or even suppress the fingering instability, but it also makes the system susceptible to additional solid-mechanical instabilities. We show that in elastic-walled Hele-Shaw cells that are bounded by sufficiently thin elastic sheets the (fluid-based) viscous fingering instability can arise concurrently with a (solid-based) wrinkling instability. We study the interaction between these distinct instabilities, using a theoretical model that couples the depth-averaged lubrication equations for the fluid flow to the Föppl–von Kármán equations which describe the deformation of the thin elastic sheet. We employ a linear stability analysis to determine the growth rate of non-axisymmetric perturbations to the axisymmetrically expanding bubble and perform direct numerical simulations to study the nonlinear interactions between the instabilities. We show that system’s behaviour may be characterised by a non-dimensional parameter that indicates the strength of the fluid-structure interaction. For small [large] values of this parameter the system’s behaviour is dominated by viscous fingering [wrinkling], with strong interactions between the two instabilities arising in an intermediate regime.

I. INTRODUCTION

Fluid-structure interaction plays an important role in many industrial and natural processes ranging in scale from spreading magma underneath deforming strata^{22,23} to elasto-capillary instabilities in the small airways of the lung¹⁴. Compliant boundaries can provide an effective means of suppressing fluid mechanical instabilities, e.g. in the suppression of boundary layer instabilities by compliant surfaces⁹, or the suppression of ribbing instabilities by elastomer-coated rolls^{2,3}. However, the fluid loading acting on the elastic boundaries can also induce structural instabilities. Examples include the elasto-capillary buckling of compliant parts in MEMS devices³² which leads to clustering similar to the clumping of hairs in a paintbrush¹ or bird feathers in the rain¹⁰. In this paper, we explore the interaction between fluid- and solid-mechanical instabilities which can arise concurrently when air displaces a viscous liquid in the narrow gap between a rigid plate and an elastic membrane – the elastic-walled Hele-Shaw cell.

Viscous fingering in rigid-walled Hele-Shaw cells is an archetype for front-propagating, pattern forming phenomena^{4,25,31}. When air is injected into the narrow, liquid-filled gap between parallel rigid plates, the axisymmetrically expanding air-liquid interface tends to be unstable to non-axisymmetric perturbations when the capillary number – the ratio of (destabilising) viscous to (stabilising) capillary forces acting at the air-liquid interface – becomes sufficiently large. Small-amplitude initial perturbations to the unstable axisymmetric air-liquid interface grow rapidly into large-amplitude fingers. These in turn become unstable to tip-splitting which, in combination with the arrest of the interface after the passage of the finger tips, leads to the formation of complex, highly branched patterns such as those shown in Fig. 1(a).

A recent experimental study by Pihler-Puzović *et al.*²⁶ demonstrated that the onset of viscous fingering can be delayed considerably when the upper bounding plate of the Hele-Shaw cell is replaced by an elastic membrane, as illustrated in Fig. 1 where the expanding air-liquid interface remains axisymmetric (Fig. 1(b)) for a value of the injection flow rate at which the rigid system (Fig. 1(a)) already exhibits strong nonlinear growth. Pihler-Puzović *et al.*'s²⁷ subsequent theoretical analysis identified the dominant mechanisms by which fluid-structure interaction weakens (or even suppresses) the viscous fingering instability. The key feature of flow in elastic-walled Hele-Shaw cells is that the injection of air results in the

transverse deflection of the flexible upper boundary. This slows down the axisymmetric expansion of the air bubble (compared to a bubble growing in the corresponding rigid-walled system) and thus weakens the destabilising viscous effects. Furthermore, in an elastic-walled cell the air-liquid interface propagates into a narrowing fluid-filled gap, implying that the protruding fingers experience a higher viscous resistance compared to the rest of the interface, which reduces their growth rate. Pihler-Puzović *et al.*²⁷ characterised the importance of fluid-structure interaction in terms of a non-dimensional parameter, \mathcal{I} , the ratio of the typical viscous stresses in the fluid to the bending stiffness of the elastic membrane. They showed that an increase in \mathcal{I} (corresponding to a reduction in the membrane’s Young’s modulus while keeping all other parameters, such as the injection flow rate, constant) reduces the growth rate of the viscous fingering instability. Fingering instabilities can still develop in elastic-walled cells (at higher injection flow rates) but the nonlinear growth of the instability now results in the formation of “short, stubby fingers” (see Fig. 1(c)) instead of the complex, highly branched patterns observed in rigid-walled cells. In the experiments²⁶ and in numerical simulations of the problem²⁷ the elastic membrane was found to remain approximately axisymmetric even when the air-liquid interface developed large-amplitude fingers. However, more recent experiments in which the latex sheets used in the original study²⁶ were replaced by much thinner polypropylene membranes showed clear evidence of non-axisymmetric buckling. This solid-based instability interacted strongly with the fluid-mechanical viscous fingering instability, as shown in Fig. 1(d).

Buckling of thin-walled elastic sheets is typically associated with the presence of compressive in-plane stresses²⁰. Once these stresses exceed a certain threshold, it becomes energetically favourable for the membrane to adopt a non-axisymmetrically buckled configuration because the increase in strain energy associated with bending becomes less than that associated with any further in-plane compression. Thinner sheets are generally more susceptible to buckling because a decrease in their thickness, h , reduces their bending stiffness, $K = Eh^3/(12(1 - \nu^2))$ (where E and ν are the sheet’s Young’s modulus and Poisson ratio, respectively), more rapidly than their extensional stiffness, $D = Eh/(1 - \nu^2)$. During the initial stages of the buckling process, sheets tend to deform in small-amplitude, periodic wrinkling patterns^{8,11,16,35}. An increase in the amplitude of the deformation frequently triggers secondary bifurcations which result in the emergence of a smaller number of large-amplitude “folds” from the initial wrinkling pattern. These folds are strongly bent regions

which localise the strain in order to reduce the overall strain energy in the system^{15,18,28,33}.

There are many systems in which fluid forces acting on thin membranes can cause wrinkling. For instance, capillary stresses can induce wrinkling instabilities in membranes that are placed on a liquid drop¹⁸, or are deformed by a small drop that is deposited on their surface^{17,34}. Conversely, the wrinkling of elastic sheets in response to external (non-fluid-mechanical) forces can cause the non-axisymmetric deformation of the air-liquid interface, as in the blistering problem studied by Chopin *et al.*⁵ who analysed the quasi-steady evolution of a small air bubble formed in a thin layer of viscous fluid underneath a wrinkling sheet.

The key feature of the current study is that the development of wrinkling instabilities in thin-walled elastic Hele-Shaw cells involves two distinct fluid- and solid-based instabilities (viscous fingering and wrinkling, respectively) which can arise concurrently and then interact strongly with each other. We study the onset of and the nonlinear interactions between these instabilities using a combination of linear stability analysis and direct numerical simulations. The outline of the paper is as follows: In section II we describe our theoretical model which is based on the depth-averaged lubrication equations, coupled to the Föppl–von Kármán equations which describe the deformation of the elastic membrane. We discuss the linear stability of the axisymmetrically evolving system in section III, before analysing the nonlinear interaction between the fingering and wrinkling instabilities by direct numerical simulations in section IV. We conclude with a summary and a discussion of our findings in section V.

II. THE MODEL

We consider a circular Hele-Shaw cell of radius R_{outer} whose upper boundary is formed by an elastic membrane of thickness h , Young’s modulus E and Poisson’s ratio ν ; see Fig. 1(e), (f). When the membrane is in its undeformed configuration, the cell has a uniform depth $b_0 \ll R_{\text{outer}}$, so the aspect ratio of the cell is small, $\mathcal{A} = b_0/R_{\text{outer}} \ll 1$. Air is injected at a constant flow rate \dot{V} at the centre of the cell (at $r^* = 0$) and displaces the viscous fluid (of dynamic viscosity μ and surface tension γ) that occupies the region Ω_{fluid} . The sheet deforms in response to the pressure in the fluid, p^* , and the spatially constant pressure in the air bubble, $p_B^*(t)$, thereby changing the depth of the Hele-Shaw cell, b^* . If the resulting vertical deflection of the membrane, w^* , becomes comparable to the membrane’s thickness,

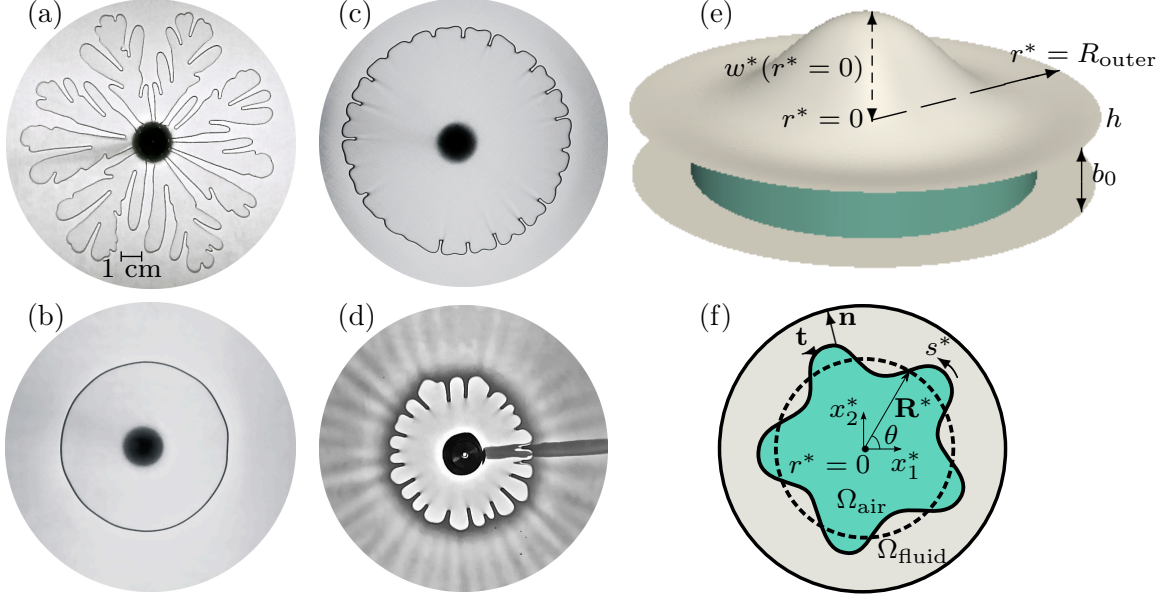


FIG. 1. Top view of the experimental fingering patterns²⁶ in (a) the rigid cell; (b, c) the elastic-walled cell with a latex membrane of thickness $h = 0.33$ mm and Young's modulus $E = 1.44$ MPa; and (d) the elastic-walled cell with a polypropylene membrane of thickness $h = 30$ μm and Young's modulus $E = 3.6$ GPa, in which a growing air bubble displaces silicone oil at a constant injection flow rate (a, b) $\dot{V} = 145$ ml min⁻¹ and (c, d) $\dot{V} = 1.25$ l min⁻¹. The latex and polypropylene sheets have approximately the same bending stiffness, $K = 0.57 \times 10^{-5}$ kg m² sec⁻² and 1.08×10^{-5} kg m² sec⁻², respectively. Diagram of the elastic-walled Hele-Shaw cell: (e) perspective view and (f) top view. All quantities are given in dimensional variables.

the self-induced in-plane stresses make an important contribution to the elastic response of the flexible wall and wrinkling of the sheet is possible²⁰.

We non-dimensionalise the problem as follows:

$$[x_1^*, x_2^*, r^*, w^*] = [x_1, x_2, r, w] R_{\text{outer}}, \quad b = b^*/b_0, \quad [p_B^*, p^*] = [p_B, p] \mathcal{P}, \quad t^* = t \mathcal{T},$$

where $\mathcal{T} = 2\pi R_{\text{outer}}^2 b_0 / \dot{V}$ and $\mathcal{P} = 6\mu\dot{V} / \pi b_0^3$ are the natural time and pressure scales for flux-driven flow in the narrow gap between the walls of the cell, respectively. Throughout the paper a superscript ‘*’ is used to distinguish dimensional quantities from their non-dimensional equivalents.

We describe the flow of the viscous fluid by the non-dimensional Reynolds lubrication

equation²⁹,

$$\frac{\partial b}{\partial t} = \nabla \cdot (b^3 \nabla p) \quad \text{in } \Omega_{\text{fluid}}, \quad (1)$$

subject to the kinematic boundary condition at the air-liquid interface

$$\frac{\partial \mathbf{R}}{\partial t} \cdot \mathbf{n} = -b^2 \nabla p \cdot \mathbf{n} \quad \text{at } \partial\Omega_{\text{air}}, \quad (2)$$

where the vector $\mathbf{R} = \mathbf{R}^*/R_{\text{outer}} = R(\theta, t) \mathbf{e}_r$ describes the position of the interface and \mathbf{n} is the unit normal pointing into the viscous fluid. Surface tension induces a pressure jump over the curved air-liquid interface, implying that

$$p_B(t) - p = \frac{1}{12} Ca^{-1} \mathcal{A} (\kappa_{\parallel} + \kappa_{\perp}) = \frac{1}{12} Ca^{-1} \mathcal{A} \left(\mathcal{A} \frac{\partial \mathbf{t}}{\partial s} \cdot \mathbf{n} + \frac{2}{b} \right), \quad (3)$$

where $Ca = \mu R_{\text{outer}}/\gamma\mathcal{T}$ is the capillary number, κ_{\parallel} and κ_{\perp} are the in-plane and transverse interface curvatures, and \mathbf{t} is the unit tangent to the air-liquid interface (in the plane of the Hele-Shaw cell) pointing in the direction of an increase in the arclength $s = s^*/R_{\text{outer}}$; see Fig. 1(f). We assume that the pressure at the outer edge of the Hele-Shaw cell is atmospheric and set

$$p(r = 1) = 0. \quad (4)$$

Mass conservation for the volume of air in the bubble region, Ω_{air} , requires that

$$\int_{\Omega_{\text{air}}(t)} b(x_1, x_2, t) dx_1 dx_2 = \int_{\Omega_{\text{air}}(t=0)} b(x_1, x_2, t=0) dx_1 dx_2 + 2\pi t. \quad (5)$$

We describe the deformation of the membrane by the non-dimensional Föppl-von Kármán equations²⁰:

$$\nabla^4 w - \eta \left[\frac{\partial^2 \phi}{\partial x_2^2} \frac{\partial^2 w}{\partial x_1^2} + \frac{\partial^2 \phi}{\partial x_1^2} \frac{\partial^2 w}{\partial x_2^2} - 2 \frac{\partial^2 \phi}{\partial x_1 \partial x_2} \frac{\partial^2 w}{\partial x_1 \partial x_2} \right] = \begin{cases} \mathcal{I} p_B & \text{in } \Omega_{\text{air}}, \\ \mathcal{I} p & \text{in } \Omega_{\text{fluid}}, \end{cases} \quad (6)$$

$$\nabla^4 \phi + \left[\frac{\partial^2 w}{\partial x_1^2} \frac{\partial^2 w}{\partial x_2^2} - \left(\frac{\partial^2 w}{\partial x_1 \partial x_2} \right)^2 \right] = 0, \quad (7)$$

where $\phi = \phi^*/(EhR_{\text{outer}}^2)$ is an Airy stress function for the in-plane stresses in the membrane (such that $\sigma_{11} = \partial^2 \phi / \partial x_2^2$, $\sigma_{22} = \partial^2 \phi / \partial x_1^2$ and $\sigma_{12} = -\partial^2 \phi / \partial x_1 \partial x_2$). The parameter $\eta = 12(1 - \nu^2)(R_{\text{outer}}/h)^2 = (1 - \nu^2)R_{\text{outer}}^2 D/K$ controls the relative importance of in-plane and bending stresses. We note that for $|w^*| \ll h$, the nonlinear terms in the Föppl-von

Kármán equations can be neglected, reducing equations (6) - (7) to the classical linear plate-bending model

$$\nabla^4 w = \begin{cases} \mathcal{I} p_B & \text{in } \Omega_{\text{air}}, \\ \mathcal{I} p & \text{in } \Omega_{\text{fluid}}. \end{cases}$$

The parameter $\mathcal{I} = 12\mu\dot{V}/(2\pi\mathcal{A}^3K)$ is the ratio of the typical viscous stresses in the fluid to the bending stiffness of the elastic membrane and therefore provides a measure of the importance of the fluid-structure interaction; as $\mathcal{I} \rightarrow 0$ the system's behaviour approaches that of a rigid-walled Hele-Shaw cell. The deflection of the membrane affects the depth of the Hele-Shaw cell in (1), (2), (3) and (5) via

$$b = 1 + w/\mathcal{A}. \quad (8)$$

We assume the membrane to be clamped and free of any in-plane stresses at its outer boundary:

$$w = 0, \quad \frac{\partial w}{\partial n} = 0, \quad \phi = 0, \quad \frac{\partial \phi}{\partial n} = 0 \quad \text{at } \partial\Omega_{\text{fluid}}. \quad (9)$$

The problem (1)-(9) is governed by four non-dimensional parameters: the aspect ratio \mathcal{A} , the capillary number Ca , the Föppl-von Kármán parameter η , and the fluid-structure interaction (FSI) parameter \mathcal{I} . Throughout this paper, we use the same parameter values for the aspect ratio and the capillary number as in our previous study²⁷ ($\mathcal{A} = 0.04$ and $Ca^{-1} = 2.5$), but we increase the Föppl-von Kármán parameter from $\eta = 10^2$ to $\eta = 2 \times 10^6$, corresponding to a reduction the sheet's thickness. We study the system's behaviour by varying the FSI parameter \mathcal{I} (which corresponds to changing the Young's modules of the sheet if all other parameters are kept constant) to assess the effect of fluid-structure interaction on the fingering and wrinkling instabilities.

III. AXISYMMETRIC EVOLUTION AND LINEAR STABILITY TO NON-AXISYMMETRIC PERTURBATIONS

We start by studying the axisymmetric evolution of the system. Inserting the ansatz $p = \bar{p}(r, t)$, $w = \bar{w}(r, t)$, $\phi = \bar{\phi}(r, t)$ and $R = \bar{R}(t)$ into the equations in section II transforms them into a spatially one-dimensional system of partial differential equations²⁷. Representative numerical results obtained from the time integration of these equations for $\mathcal{I} = 10^4$ starting

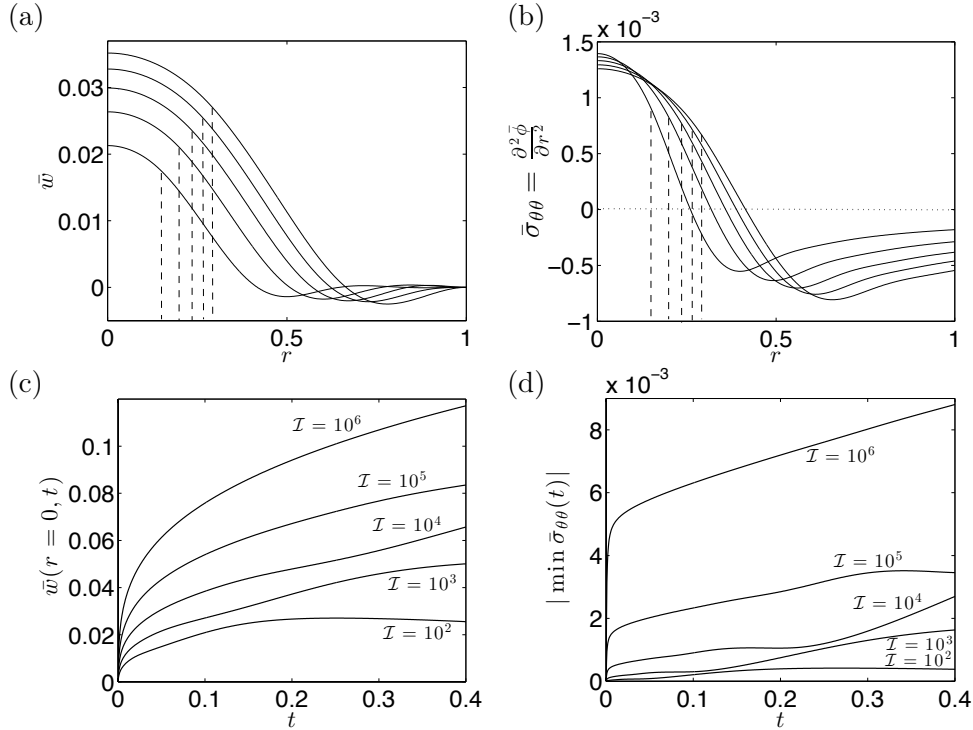


FIG. 2. Plots illustrating the system’s axisymmetric evolution by showing (a) the membrane profiles and (b) azimuthal stresses, at $t = 0.016, 0.031, 0.046, 0.061$ and 0.076 , for $\mathcal{I} = 10^4$. The dashed lines indicate the position of the air-liquid interface at the given times. (c) The inflation of the membrane at the centre of the cell, $\bar{w}(r = 0, t)$, and (d) the absolute value of the maximum compressive stresses, $|\min \bar{\sigma}_{\theta\theta}(t)|$, versus time, t , for a range of FSI parameters \mathcal{I} .

from an initially flat, undeformed membrane ($\bar{w}(r, t = 0) = 0$) and a bubble radius of $\bar{R}(t = 0) = R_{\text{init}} = 0.05$ are shown in Fig. 2. The plots of the membrane deflection and the position of the air-liquid interface (at five equally-spaced instants) in Fig. 2(a) are qualitatively similar to those observed for the case of smaller η considered in reference²⁷: the injection of air at $r = 0$ not only displaces the viscous fluid but also inflates the bounding membrane, more so for larger values of \mathcal{I} ; see the plot of the membrane’s deflection at its centre, $\bar{w}(r = 0, t)$, in Fig. 2(c).

The plot of the azimuthal membrane stresses, $\bar{\sigma}_{\theta\theta}$, in Fig. 2(b) indicates that they become compressive ($\bar{\sigma}_{\theta\theta} < 0$) at a certain distance ahead of the air-liquid interface, suggesting that this region may be susceptible to wrinkling instabilities. Since the maximum compressive stress (or $|\min \bar{\sigma}_{\theta\theta}(t)|$) increases with an increase in \mathcal{I} (see Fig. 2(d)) the system’s stability to non-axisymmetric perturbations is therefore affected by two competing effects: while an

increase in \mathcal{I} weakens the viscous fingering instability²⁷ it is likely to increase the membrane's propensity to wrinkle.

To assess the linear stability of the evolving axisymmetric base state to non-axisymmetric perturbations (arising through viscous fingering or the wrinkling of the membrane), we substituted the ansatz $p = \bar{p}(r, t) + \varepsilon \hat{p}_N(r, t) \cos(N\theta)$, $w = \bar{w}(r, t) + \varepsilon \hat{w}_N(r, t) \cos(N\theta)$, $\phi = \bar{\phi}(r, t) + \varepsilon \hat{\phi}_N(r, t) \cos(N\theta)$, $R = \bar{R}(t) + \varepsilon \hat{R}_N(t) \cos(N\theta)$ into the equations of section II and linearised with respect to the amplitude $\varepsilon \ll 1$. This results in another system of spatially one-dimensional partial differential equations which contain the azimuthal wavenumber N as a parameter. These equations were again solved numerically starting from the initial conditions of $\hat{w}_N(r, t = 0) = 0$, which correspond to an initially flat, undeformed membrane, and a non-zero value for \hat{R}_N , which imposes a small non-axisymmetric perturbation (with wavenumber N) to the bubble radius. This procedure mimics the protocol employed in the experiments²⁶.

Typical results of the linear stability analysis are shown in Fig. 3(a) where we plot the amplitude of the perturbation to the air-liquid interface, \hat{R}_N , as a function of the bubble's mean radius, \bar{R} , for wavenumbers in the range $N \leq 20$ and for $\mathcal{I} = 10^4$. The lines are thickened where the growth rate of perturbations, given by $1/\hat{R}_N d\hat{R}_N/dt$, is negative. The lines in Fig. 3(a) show that the initial configuration (for which $\bar{R} = R_{\text{init}} = 0.05$) is already unstable to non-axisymmetric perturbations: for modes with $N \leq 9$, the perturbation amplitude \hat{R}_N grows immediately while perturbations with higher wavenumbers decay, at least during the early stages of the system's evolution. The growth rates generally vary with \bar{R} and modes that are initially stable can become unstable when the bubble has grown to a larger mean radius; see, e.g., the $N = 10$ mode whose amplitude decays initially but increases when $\bar{R} \gtrsim 0.081$. (Note that, to facilitate the interpretation of the figure, the line thickness is increased in regimes where the growth rate of the non-axisymmetric instability is negative).

A significant new feature in Fig. 3(a), not seen in the simulations for smaller values of η , is the sudden onset of powerful instabilities for modes with larger wavenumbers, indicated by the rapidly growing magnitude of \hat{R}_N for modes with $N \geq 10$ at larger values of \bar{R} . (The change in the sign of \hat{R}_N indicates that, compared to the initial perturbation applied at $t = 0$, the instability has inverted the non-axisymmetric deflection of the the air-liquid interface, with “finger”-tips becoming bases and vice versa). We suspect these instabilities

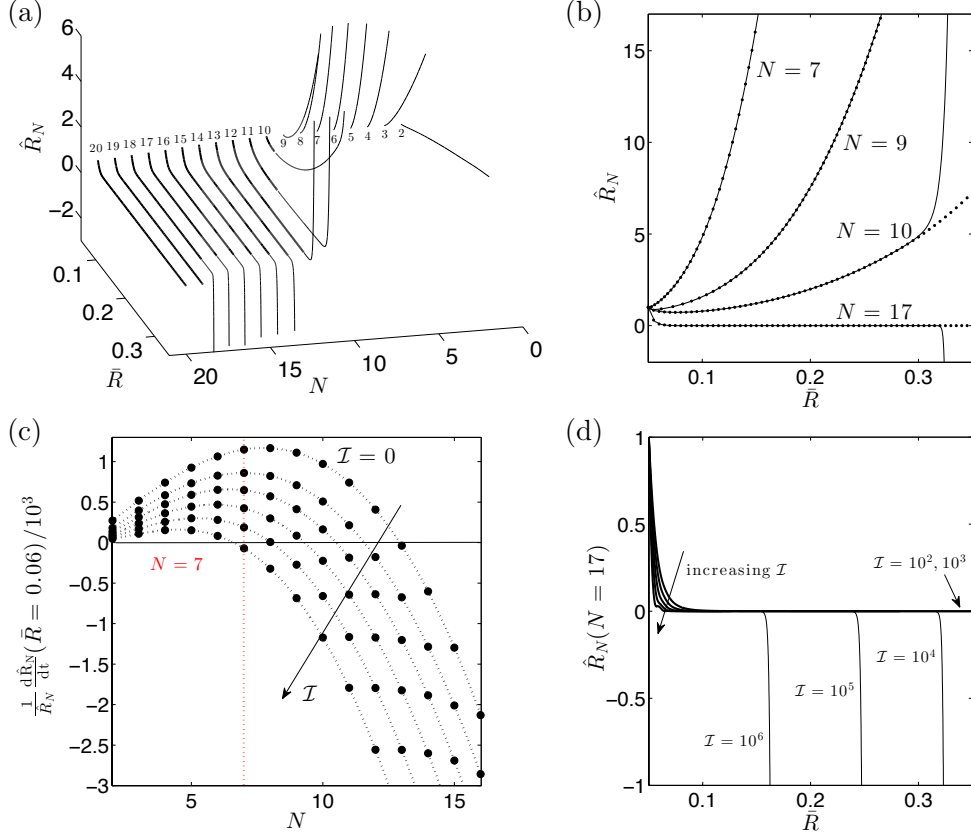


FIG. 3. (a) Evolution of the amplitude of the non-axisymmetric perturbation, \hat{R}_N , as a function of the bubble's mean radius, \bar{R} , for wavenumbers N between 2 and 20. (b) Evolution of the amplitude of the non-axisymmetric perturbation \hat{R}_N as a function of the radius \bar{R} for selected wavenumbers N , obtained in the full problem (solid lines) and when ignoring non-axisymmetric perturbations to the wall shape by setting $\hat{w}_N = \hat{\phi}_N = 0$ (dotted lines). In (a) and (b) $\mathcal{I} = 10^4$. (c) The growth rates, $1/\hat{R}_N d\hat{R}_N/dt$, at a fixed radius $\bar{R} = 0.06$ as a function of the wavenumber N for $\mathcal{I} = 0, 10^2, 10^3, 10^4, 10^5$ and 10^6 . The direction of increasing \mathcal{I} is indicated by the arrow. (d) Evolution of the amplitude of the non-axisymmetric perturbation \hat{R}_N as a function of the radius \bar{R} for $N = 17$ and values of the FSI parameter \mathcal{I} indicated in the plot. In (a) and (d) the lines are thickened in regions where the amplitude of the perturbation decays.

to be associated with the wrinkling of the membrane. To verify this, we suppressed the non-axisymmetric deformations of the elastic membrane by setting $\hat{\phi}_N = \hat{w}_N = 0$ and repeated the stability analysis. The results are shown in Fig. 3(b) where we contrast the evolution of the amplitudes \hat{R}_N (for $N = 7, 9, 10$ and 17) obtained from the linear stability analysis, allowing (solid lines) and suppressing (dotted lines) non-axisymmetric membrane

deformations. During the early stages of the system's evolution, the predictions from the two analyses agree extremely well, indicating that the instability arises through viscous fingering whose onset does not require (and is only affected very little by) non-axisymmetric perturbations to the wall shape. Conversely, the rapidly growing instabilities that develop at larger values of \bar{R} for perturbations with higher wavenumbers are suppressed by setting the non-axisymmetric membrane displacements to zero, indicating that they are closely linked to the wrinkling of the membrane.

Since wrinkling is associated with the development of compressive azimuthal stresses, we note that the membrane can withstand considerable compression without wrinkling. This is illustrated in the plots showing the instantaneous spatial distribution of $\bar{\sigma}_{\theta\theta}$ at five equally-spaced instants in the system's axisymmetric evolution in Fig 2(b). The plots cover the period during which the axisymmetric state becomes linearly unstable to wrinkling and show that $\bar{\sigma}_{\theta\theta}$ already reaches considerable negative values before the onset wrinkling.

Fig. 3(c) shows the effect of variations in the FSI parameter \mathcal{I} on the growth rate of the non-axisymmetric instabilities at a fixed, relatively small radius of $\bar{R} = 0.06$, i.e. in a regime in which the instabilities arise exclusively through the viscous fingering mechanism. Qualitatively, the behaviour is very similar to that found in the simulations with smaller values of η : an increase in \mathcal{I} weakens the non-axisymmetric instabilities and reduces their most unstable wavenumber. For instance, for $\mathcal{I} = 10^6$, the $N = 7$ mode (the fastest-growing mode in the initial configuration for $\mathcal{I} = 0$) has become stable and the most unstable wavenumber has been reduced to $N = 5$. We note that typically a range of unstable modes have similar growth rates.

Fig. 3(d) illustrates the effect of variations in \mathcal{I} on the wrinkling instabilities by plotting the evolution of \hat{R}_N for $N = 17$: an increase in \mathcal{I} increases the decay rate of the (viscous fingering) instabilities at small values of \bar{R} but ultimately leads to an earlier onset of wrinkling.

IV. DIRECT NUMERICAL SIMULATIONS

The results of the linear stability analysis indicate that the axisymmetrically evolving system is susceptible to non-axisymmetric instabilities which arise through two distinct physical mechanisms (viscous fingering and membrane wrinkling). Furthermore, in any given

axisymmetric configuration the system is typically unstable to perturbations with a range of wavenumbers. Once these instabilities have grown to finite amplitude the system’s overall behaviour is likely to be determined by nonlinear interactions between various unstable modes. We shall now explore these interactions by direct numerical simulations, using an `oomph-lib`¹³-based finite element discretization of the governing equations²⁷. As in the case of the linear stability analysis in section III we started the simulations from a configuration with zero wall displacement, $w(r, t = 0) = 0$, and an initial bubble radius of $\bar{R}(t = 0) = R_{\text{init}} = 0.05$. We perturbed the bubble radius by a small non-axisymmetric perturbation with an amplitude of 1% of the initial radius.

A. Variations in the FSI parameter \mathcal{I}

We start by analysing the system’s behaviour by varying the FSI parameter \mathcal{I} while keeping all other non-dimensional parameters, including the wavenumber of the initial perturbation, constant: throughout this section we set it to $N = 7$ – the most unstable wavenumber in the rigid cell. The effect of variations in N is then considered in section IV B.

1. $\mathcal{I} = 0$: *Highly branched fingering in rigid cells*

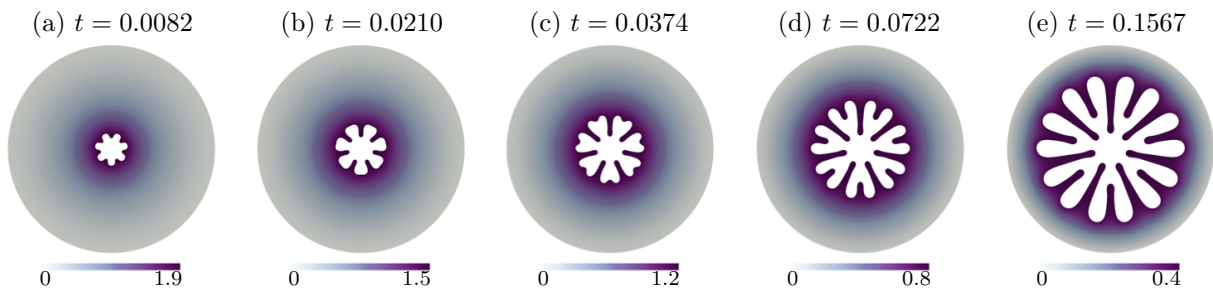


FIG. 4. Rigid cell: time evolution of the air-liquid interface and the corresponding instantaneous pressure field in the viscous fluid for $\mathcal{I} = 0$.

The development of the viscous fingering instability in the rigid-walled Hele-Shaw cell (for $\mathcal{I} = 0$) is shown in Fig. 4, using snapshots of the evolving fluid domain, with colour contours indicating the spatial variations in the fluid pressure. The small initial perturbations to the air-liquid interface grow rapidly into large-amplitude fingers whose tips split when the tips

become sufficiently wide¹⁹. The pressure gradient in the thin “fjords” of fluid that separate the propagating fingers is small, implying that the fluid in these regions only moves very slowly. Tip splitting combined with the arrest of the interface after the passage of the finger tips results in the formation of the characteristic highly branched pattern.

2. $\mathcal{I} = 10^2$: Weakening of fingering instability; no buckling

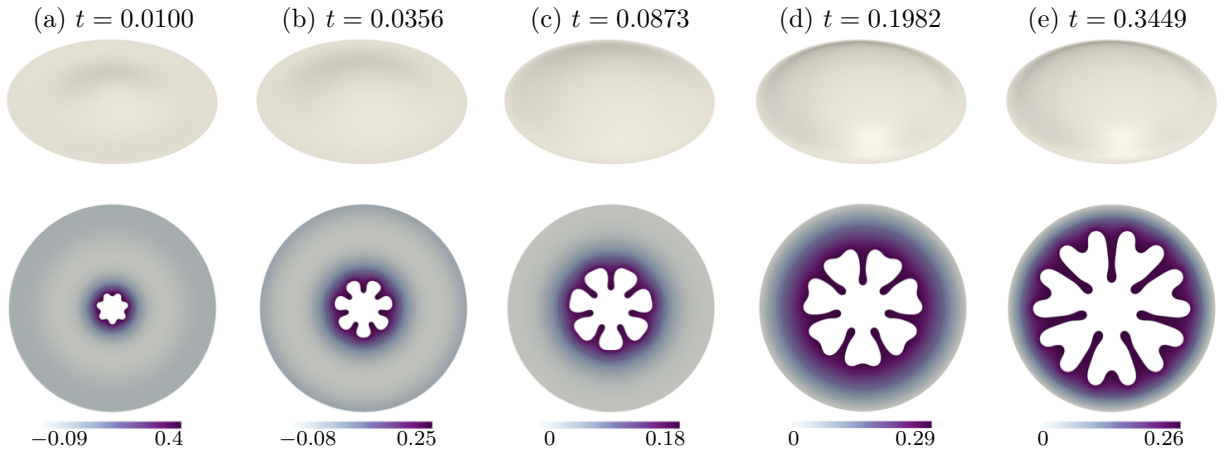


FIG. 5. No wrinkling: time evolution of the air-liquid interface, the corresponding instantaneous pressure fields in the viscous fluid and a perspective view of the sheet deformations (with the transverse displacement increased by a factor of 10) for $\mathcal{I} = 10^2$.

The plots in Fig. 5 show the corresponding results for an elastic-walled cell with $\mathcal{I} = 10^2$. The inflation of the membrane (whose deformation is illustrated by the plots in the top row of that figure) not only reduces the rate at which the bubble expands, but also decreases the growth rate of the fingering instability and delays the occurrence of tip-splitting. Furthermore, the bases of the fingers continue to propagate outwards, resulting in the shortening of the “fjords”. As a result the finger shapes begin to bear a closer resemblance to the “short and stubby” patterns observed in the experiments with elastic-walled sheets than the highly branched pattern shown in Fig. 4. Even though the large-amplitude non-axisymmetric displacement of the air-liquid interface creates a highly non-uniform pressure load on the elastic membrane its deformation remains approximately axisymmetric throughout the system’s evolution.

3. $\mathcal{I} = 10^3$: *Passive buckling*

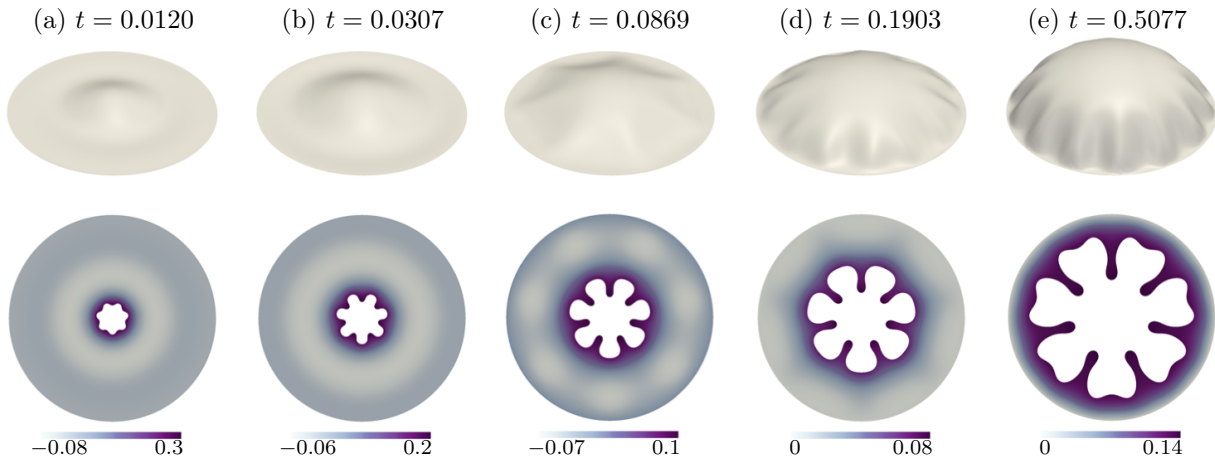


FIG. 6. Passive buckling: time evolution of the air-liquid interface, the corresponding instantaneous pressure fields in the viscous fluid and the sheet deformations (with the transverse displacement increased by a factor of 10) for $\mathcal{I} = 10^3$.

An increase of \mathcal{I} to 10^3 results in larger membrane deflections and a further reduction in the growth rate of the viscous fingering instability. The membrane remains approximately axisymmetric until the bubble has grown to a mean radius of $\bar{R} \approx 0.275$. Beyond this, the membrane buckles with a wavenumber that matches the number of viscous fingers ($N = 7$; see Fig. 6(c)), suggesting that the non-axisymmetric deformation of the membrane is a passive response to the fingering instability. As the system evolves further, the interaction of the structural instability with the cell boundary results in a doubling of the number of creases to $N = 14$; see Fig. 6(d-e). We note that this increase does not arise as a passive response to the tip-splitting at the air-liquid interface which only occurs much later in the system's evolution. See, e.g., Fig. 6(d) where the number of creases has already doubled while the finger tips show no signs of splitting yet. We refer to reference³³ for an analysis of this process.

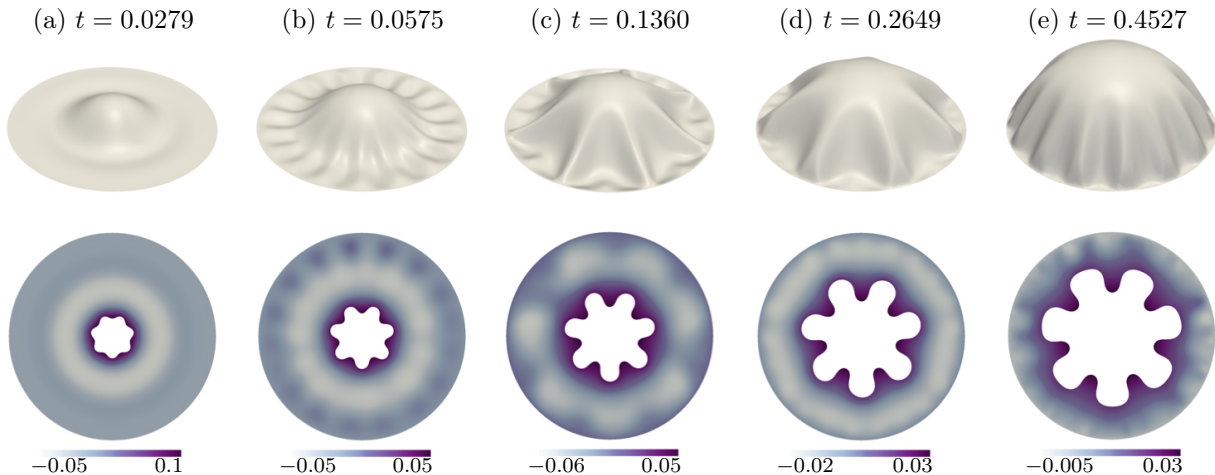


FIG. 7. Fingering controls wrinkling: time evolution of the air-liquid interface, the corresponding instantaneous pressure fields in the viscous fluid and the sheet deformations (with the transverse displacement increased by a factor of 10) for $\mathcal{I} = 10^4$.

4. $\mathcal{I} = 10^4$: *Fingering controls buckling*

Increasing \mathcal{I} to 10^4 introduces a key new feature to the problem (Fig. 7). Though the fingers now grow even more slowly, the air-liquid interface is still unstable to non-axisymmetric perturbations with wavenumber $N = 7$, but the membrane no longer responds passively to the fingering instability. Instead it first wrinkles with a different (and incommensurate) wavenumber of $N = 17$ (Fig. 7(b)). This suggests that the initial buckling of the sheet now arises via a distinct solids-based instability in the region ahead of the air-liquid interface where the membrane is subject to compressive azimuthal stresses. Nonlinear interaction between the two instabilities then re-adjusts the membrane deformation to a pattern with $N = 7$ dominant creases (Fig. 7(c)), matching the number of viscous fingers. The subsequent evolution of the system is similar to that observed for $\mathcal{I} = 10^3$, with the number of creases doubling as the buckling pattern begins to interact with the boundary (Fig. 7(d-e)). In terms of the terminology used in studies of buckling in thin elastic membranes^{15,28}, the evolution of the membrane’s shape when the wrinkling pattern approaches the boundary may be interpreted as the transition from a state that is best described as “wrinkling” (characterised by the presence of small-amplitude, smooth undulations of the elastic sheet; Fig. 7(b)), to “folding” (a state in which a smaller number of dominant creases with strongly bent regions

emerges from the initial wrinkling pattern; Fig. 7(c)). While the changes to the membrane shape in this regime are therefore likely to have their origin in the solid mechanics, the development of the folds is clearly influenced by the nonlinear interactions with the viscous fingering instability which determines the number of folds that ultimately emerge from the process.

5. $\mathcal{I} = 10^5$: *Buckling interacts with fingering*

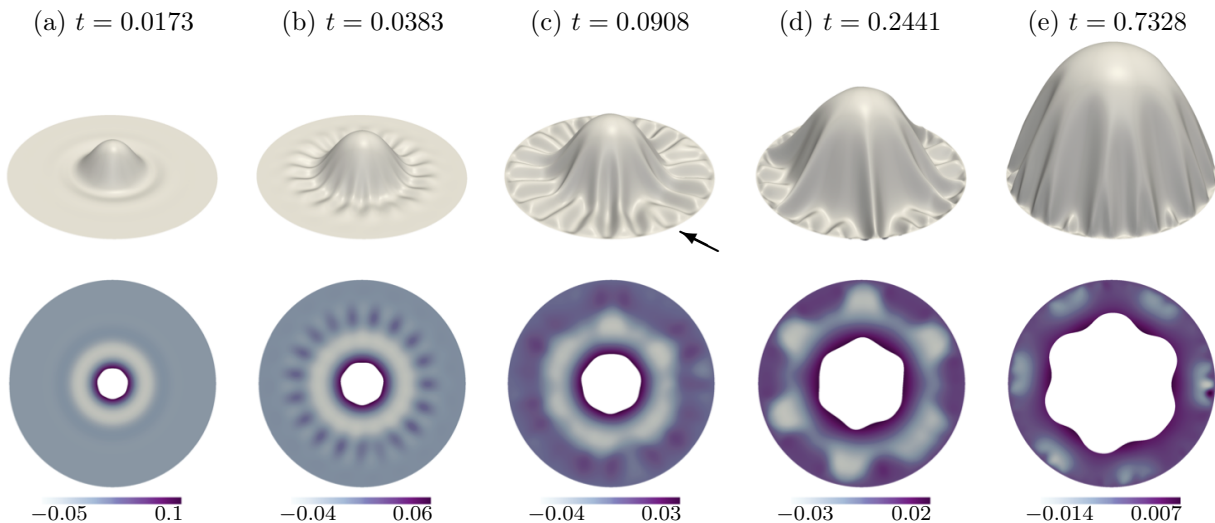


FIG. 8. Wrinkling alters fingering: time evolution of the air-liquid interface, the corresponding instantaneous pressure fields in the viscous fluid and the sheet deformations (with the transverse displacement increased by a factor of 10) for $\mathcal{I} = 10^5$. The arrow indicates the region of the small-scale frustration in the pattern.

Fig. 8 illustrates the effect of a further increase in \mathcal{I} to 10^5 . In this case the fingering instability has become so weak that the non-axisymmetric perturbation to the air-liquid interface that we initiated with a wavenumber of $N = 7$ has grown to a barely noticeable amplitude when wrinkling first occurs with its own distinct wavenumber of $N = 19$ (Fig. 8(b)). Unlike the case shown in Fig. 7 for $\mathcal{I} = 10^4$, it is clear that wrinkling is initiated in the narrow annular region where the compressive stresses are largest, without being affected by the outer boundary. The nonlinear interaction between the two instabilities now leads to an adjustment of both wavenumbers and following a complicated transition (Fig. 8(c)), a

pattern with $N = 6$ viscous fingers and a matching number of folds emerges (Fig. 8(d)). As the wrinkling pattern approaches the outer boundary the number of creases first doubles and then quadruples, but without affecting the number of fingers (Fig. 8(e)).

We note that, since the number of folds is incommensurate with the number of small-scale creases that developed during the initial wrinkling phase, the emergence of the large-scale folds is accompanied by a re-arrangement of the remaining creases. This results in the formation of irregular, small-scale frustrated patterns such as the U-shaped connection of the two creases enclosed between the two large-amplitude folds identified by the arrow in Fig. 8(c). These features are extremely delicate structures and are very sensitive to any imperfections.

6. $\mathcal{I} = 10^6$: *Buckling excites fingering*

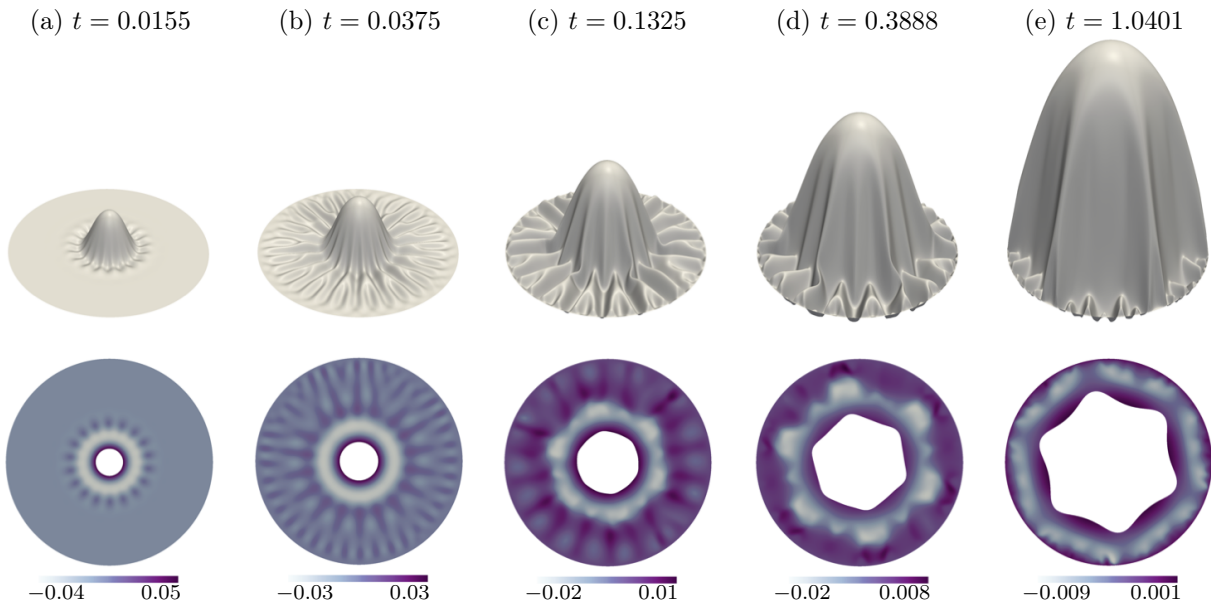


FIG. 9. Wrinkling excites fingering: time evolution of the air-liquid interface, the corresponding instantaneous pressure fields in the viscous fluid and the sheet deformations (with the transverse displacement increased by a factor of 10) for $\mathcal{I} = 10^6$.

An increase of \mathcal{I} to 10^6 finally suppresses the viscous fingering instability (see, e.g., the plot of the (linear) growth rate for the $N = 7$ mode for various values of \mathcal{I} in Fig. 3(c)) and the initial perturbation to the air-liquid interface therefore decays very rapidly. The

wrinkling of the membrane (with a wavenumber of $N = 18$) is again initiated in a narrow annular region ahead of the air-liquid interface where the compressive stresses are largest (Fig. 9(a)). The wrinkling pattern then spreads outwards and creases split into two as they reach a larger radius (Fig. 9(b)), analogous to the tip splitting in the fingering instability. As the amplitude of the wrinkling pattern increases, the deformation of the membrane begins to affect the shape of the air-liquid interface which adopts a non-axisymmetric shape with $N = 6$ fingers – commensurate with the number of wrinkles ($N = 18$) near the air-liquid interface. Compared to the case of $\mathcal{I} = 10^3$ shown in Fig. 6, the roles of the two instabilities are now exactly reversed in the sense that the non-axisymmetric deformation of the air-liquid interface now arises as a passive response to the buckling of the membrane, as in the blistering problem studied by Chopin *et al.*⁵ The cascade of buckling events that is triggered when the wrinkling pattern approaches the boundary then follows the familiar pattern and, as before, does not affect the number of the viscous fingers. The air-liquid interface protrudes into the regions where the folding of the membrane has increased the gapwidth and reduced the flow resistance. The emergence of the folds is again accompanied by the formation of small-scale frustrated patterns which follow the re-arrangement of the small-scale creases.

B. Variations in the perturbation wavenumber N

The linear stability analysis presented in section III indicated that the axisymmetrically evolving system is typically unstable to non-axisymmetric perturbations with a wide range of wavenumbers, and that many of these unstable modes have comparable growth rates; see, e.g., Figs. 3(a,c). This suggests that the buckling pattern and the number of large-amplitude fingers that ultimately emerge during the system’s non-axisymmetric evolution will depend sensitively on the (dominant) wavenumber of the initial perturbation. (The random initial perturbation to the bubble shape that is likely to be present in an actual experiment would correspond to the superposition of many different Fourier modes.)

To explore the dependence of the system’s evolution on the wavenumber of the initial perturbation, we performed a final set of parameter studies in which we fixed the value of the FSI parameter to $\mathcal{I} = 10^4$ (the value for which the viscous fingering instability was found to affect the nonlinear evolution of the wrinkling process; see section IV A 4 and Fig. 7). The plots in Fig. 10 show the membrane shapes (first and third column) and the fluid domains

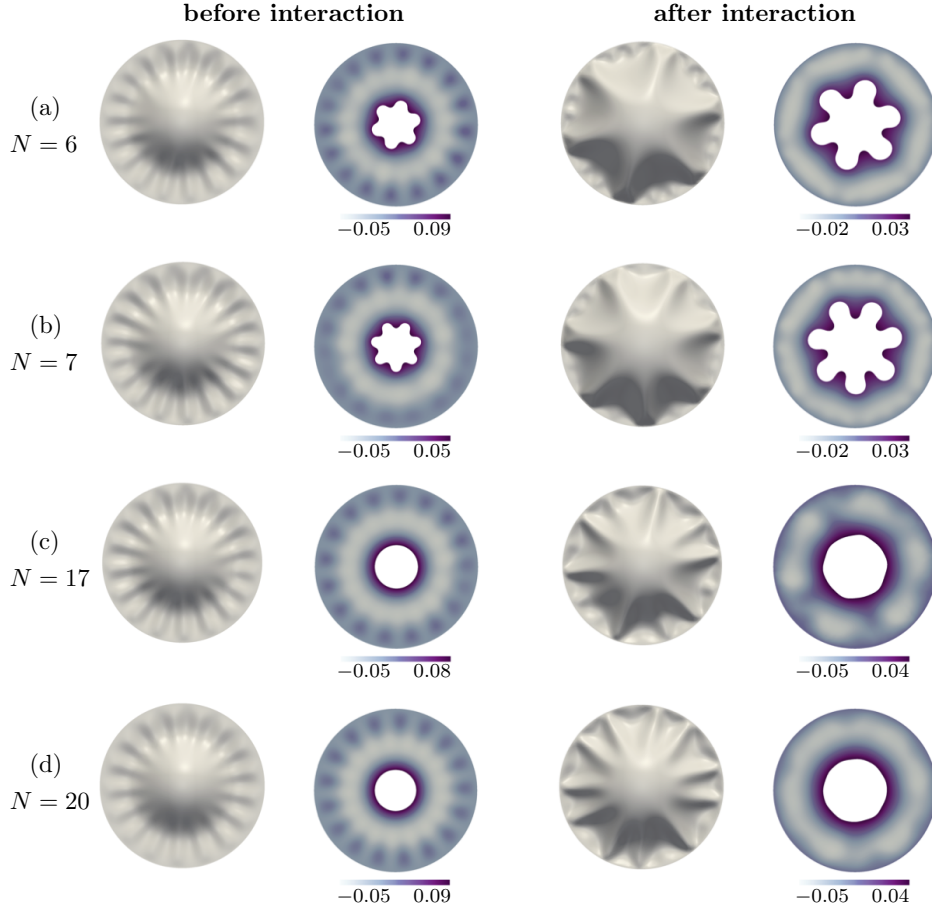


FIG. 10. Top view of the instantaneous sheet deformations and corresponding positions of the air-liquid interface and the pressure fields in the viscous fluid for $\mathcal{I} = 10^4$, before and after the interaction between wrinkling and fingering if the interface is perturbed at $t = 0$ with (a) $N = 6$, (b) $N = 7$, (c) $N = 17$ and (d) $N = 20$.

(second and fourth column) during the early stages of the system's nonlinear evolution when the two instabilities still evolve independently (first two columns), and after their interaction (last two columns), respectively.

Figs. 10(a,b) illustrate the system's evolution when perturbations with relatively small wavenumbers ($N = 6$ and $N = 7$, respectively) are applied to the air-liquid interface. The axisymmetrically evolving system is linearly unstable to perturbations with either of these wavenumbers (see Fig. 3(a)) and their growth rates only differ slightly. Figs. 10(a,b) show that the application of a small-amplitude perturbation (1% of the initial radius) to the initial shape of the bubble suffices to initiate the nonlinear growth of viscous fingers with

the wavenumber of the initial perturbation. In either case, the wrinkling instability that develops subsequently arises with its own distinct wavenumber of $N = 17$, confirming our earlier claim that the onset of wrinkling is independent of the viscous fingering instability. Conversely, the transition from membrane “wrinkling” to “folding” is clearly affected by the presence of the viscous fingers, since, following the interaction between the two instabilities, the number of folds matches the number of viscous fingers.

Figs. 10(c,d) illustrate the effect of increasing the wavenumber of the initial perturbation to values that are representative of those associated with the wrinkling of the membrane ($N = 17$ and $N = 20$). The initial configuration is stable to such perturbations (see Fig. 3(a)) and the air-liquid interface therefore returns to an axisymmetric state. The decay of the initial perturbation is, in fact, so rapid that by the time the wrinkling instability develops, the initial perturbation has very little effect on the system. The membrane wrinkles with the same wavenumber ($N = 17$) in both cases. Since the transition from “wrinkling” to “folding” is now no longer biased by the presence of any viscous fingers, the precise details of this process are extremely sensitive to the small imperfections introduced by the unstructured mesh. As a result, the overall folding pattern (which again includes many small-scale frustrated features) that emerges from the instability is qualitatively similar in both cases, though the exact details of the membrane deformation differ significantly.

V. SUMMARY AND DISCUSSION

The viscous fingering instabilities that develop readily in rigid-walled Hele-Shaw cells can be suppressed by fluid-structure interaction, introduced by replacing the upper bounding wall of the cell by an elastic membrane^{26,27}. Within our model, the importance of fluid-structure interaction is characterised by the parameter \mathcal{I} , variations in which (while keeping all other parameters constant) correspond to variations in the membrane’s Young’s modulus. An increase in \mathcal{I} increases the transverse deflection of the membrane, and weakens (and ultimately suppresses) the viscous fingering instability. However, for sufficiently thin-walled bounding membranes an increase in \mathcal{I} also increases their propensity to wrinkle, resulting in an interesting competition (and interaction) between two distinct symmetry-breaking instabilities: for small values of \mathcal{I} the system’s behaviour is dominated by viscous fingering, with the non-axisymmetric deformation of the bounding membrane arising as a passive

response to the spatial variations in the fluid pressure. In an intermediate range of \mathcal{I} , the (weakened) fingering instability initially develops independently of the wrinkling process but the two instabilities interact strongly when their amplitudes reach finite values. Finally, for large values of \mathcal{I} , viscous fingering is completely suppressed and the non-axisymmetric deformation of the expanding air-liquid interface arises as a passive response to the wrinkling of the membrane, reversing the role of the two instabilities. The change in the system's behaviour with an increase in \mathcal{I} is illustrated in the movie provided in the supplementary material²⁴ which shows a side-by-side comparison of the system's evolution for the five cases considered in section IV.

Once the bubble has grown to a sufficiently large radius, the sheet is inflated significantly and the deformation of the membrane is affected by the presence of the outer boundary. This results in the emergence of a small number of large-amplitude folds from the initial wrinkling pattern, a process that is accompanied by the formation of numerous small-scale frustrated patterns that arise through the re-arrangement of the small-amplitude creases. These structures are extremely delicate and therefore very sensitive to the small random perturbations that would be present in actual experiments, and that are here introduced by the unstructured, constantly evolving computational mesh. Like other authors who have studied similar large-amplitude wrinkling processes^{6,7,12,21,30}, we found it virtually impossible to obtain completely mesh-independent solutions in this regime, despite the fact that we employed discretisations with up to 1.5 million degrees of freedom.

Our simulations managed to capture (at least qualitatively) many of the features observed in our preliminary (and still ongoing) experiments with elastic-walled Hele-Shaw cells in which the bounding membrane is made of an extremely thin-walled polypropylene sheet. We have not yet attempted direct comparisons between simulations and experiments, partly because this would require the computations to be performed with much smaller aspect ratios. In the simulations presented here, \mathcal{A} was deliberately set to a larger value than in the experiments to reduce the number of costly-to-resolve viscous fingers²⁷. A study aimed at a direct comparison between the experiments and the theory is currently in progress.

REFERENCES

- ¹A. Boudaoud, J. Bico, and B. Roman. Elastocapillary coalescence: Aggregation and fragmentation with a maximal size. *Phys. Rev. E*, 76:060102, 2007.
- ²M. S. Carvalho and L. E. Scriven. Deformable roll coating flows: steady state and linear perturbation analysis. *J. Fluid Mech.*, 339:143–172, 1997.
- ³M. S. Carvalho and L. E. Scriven. Three-dimensional stability analysis of free surface flows: Application to forward deformable roll coating. *J. Comp. Phys.*, 151:534–562, 1999.
- ⁴J. D. Chen. Growth of radial viscous fingers in a Hele-Shaw cell. *J. Fluid Mech.*, 201:223–242, 1989.
- ⁵J. Chopin, D. Vella, and A. Boudaoud. The liquid blister test. *Proc. R. Soc. A*, 464:2887–2906, 2008.
- ⁶F. Cirak and M. Ortiz. Fully c^1 -conforming subdivision elements for finite-deformation thin-shell analysis. *Int. J. Num. Meth. Eng.*, 51:813–833, 2001.
- ⁷F. Cirak, M. Ortiz, and A. Pandolfi. A cohesive approach to thin-shell fracture and fragmentation. *Comp. Meth. Appl. Mech. Eng.*, 194:2604–2618, 2005.
- ⁸B. Davidovitch, R. D. Schroll, D. Vella, M. Adda-Bedia, and E. A. Cerda. Prototypical model for tensional wrinkling in thin sheets. *PNAS*, 108:18227–18232, 2011.
- ⁹C. Davies, P. W. Carpenter, R. Ali, and D. A. Lockerby. Disturbances development in boundary layers over compliant surfaces. In *Sixth IUTAM Symposium on Laminar-Turbulent Transition*, pages 225–230, 2006.
- ¹⁰C. Duprat, S. Protière, A. Y. Beebe, and H. A. Stone. Wetting of flexible fibre arrays. *Nature*, 482:510–513, 2012.
- ¹¹J.-C. Géminard, R. Bernal, and F. Melo. Wrinkle formation in axi-symmetrically stretched membranes. *Eur. Phys. J. E*, 15:117–126, 2004.
- ¹²H. Hedfi, A. Ghith, and H. Bel Hadj Salah. Study of dynamic drape behaviour of fabric using fem. *Int. J. Eng. Sci. Tech.*, 3:6554–6563, 2011.
- ¹³M. Heil and A. L. Hazel. `oomph-lib` – an object-oriented multi-physics finite-element library. In M. Schäfer and H.-J. Bungartz, editors, *Fluid-Structure Interaction*, pages 19–49. Springer, 2006. `oomph-lib` is available as open-source software at <http://www.oomph-lib.org>.
- ¹⁴M. Heil, A. L. Hazel, and J. A. Smith. The mechanics of airway closure. *Respiratory*

- Physiology & Neurobiology*, 163:214–221, 2008.
- ¹⁵D. P. Holmes and A. J. Crosby. Draping films: a wrinkle to fold transition. *Phys. Rev. Lett.*, 105:038303, 2010.
- ¹⁶J. Huang, B. Davidovitch, C. D. Santangelo, T. P. Russell, and N. Menon. Smooth cascade of wrinkles at the edge of a floating elastic film. *Phys. Rev. Lett.*, 105:038302, 2010.
- ¹⁷J. Huang, M. Juskiewicz, W. H. de Jeu, E. Cerda, T. Emrick, N. Menon, and T. P. Russell. Capillary wrinkling of floating thin polymer films. *Science*, 317:650, 2007.
- ¹⁸H. King, R. D. Schroll, B. Davidovitch, and N. Menon. Elastic sheet on a liquid drop reveals wrinkling and crumpling as distinct symmetry-breaking instabilities. *PNAS*, 109:9716–9720, 2012.
- ¹⁹E. Lajeunesse and Y. Couder. On the tip-splitting instability of viscous fingers. *J. Fluid Mech.*, 419:125–149, 2000.
- ²⁰L. D. Landau and E. M. Lifshitz. *Theory of elasticity, 2d ed.* Pergamon Press, 1970.
- ²¹X. Li and K. Sarkar. Front tracking simulation of deformation and buckling instability of a liquid capsule enclosed by an elastic membrane. *J. Comp. Phys.*, 227:4998–5018, 2008.
- ²²J. R. Lister, G. G. Peng, and J. A. Neufeld. Spread of a viscous fluid beneath an elastic sheet. *submitted to Phys. Rev. Lett.*, 2013.
- ²³C. Michaut. Dynamics of magmatic intrusions in the upper crust: Theory and applications to laccoliths on Earth and the Moon. *J. Geophys. Res.*, 116:B05205, 2011.
- ²⁴See supplementary material at **DOI to be inserted** for a movie that illustrates the evolution of the non-axisymmetric instabilities for the five cases considered in section IV.
- ²⁵L. Paterson. Radial fingering in a Hele-Shaw cell. *J. Fluid Mech.*, 113:513–529, 1981.
- ²⁶D. Pihler-Puzović, P. Illien, M. Heil, and A. Juel. Suppression of complex fingerlike patterns at the interface between air and a viscous fluid by elastic membranes. *Phys. Rev. Lett.*, 108:074502, 2012.
- ²⁷D. Pihler-Puzović, R. Périllat, M. Russell, A. Juel, and M. Heil. Modelling the suppression of viscous fingering in elastic-walled Hele-Shaw cells. *J. Fluid Mech. (in press)*, 2013.
- ²⁸L. Pocivavsek, R. Dellsy, A. Kern, S. Johnson, B. Lin, K. Y. C. Lee, and E. Cerda. Stress and fold localization in thin elastic membranes. *Science*, 320:912–916, 2008.
- ²⁹O. Reynolds. On the theory of lubrication and its application to Beauchamp Tower’s experiment. *Phil. Trans. Roy. Soc. Lond. A*, 117:157–234, 1886.
- ³⁰R. Rossi, M. Lazzari, R. Vitaliani, and E. Onate. Simulation of light-weight membrane

- structures by wrinkling model. *Int. J. Num. Meth. Eng.*, 62:2127–2153, 2005.
- ³¹P. G. Saffman and G. I. Taylor. The penetration of a fluid into a porous medium or Hele-Shaw cell containing a more viscous liquid. *Proc. Roy. Soc. Lond. A*, 245:312–329, 1958.
- ³²M. Taroni and D. Vella. Multiple equilibria in a simple elastocapillary system. *J. Fluid Mech.*, 712:273–294, 2012.
- ³³H. Vandeparre, M. Pineirua, F. Brau, B. Roman, J. Bico, C. Gay, W. Bao, C. N. Lau, P. M. Reis, and P. Damman. Wrinkling hierarchy in constrained thin sheets from suspended graphene to curtains. *Phys. Rev. Lett.*, 106:224301, 2011.
- ³⁴D. Vella, M. Adda-Bedia, and E. A. Cerda. Capillary wrinkling of elastic membranes. *Soft Mat.*, 6:5778–5782, 2010.
- ³⁵D. Vella, A. Ajdari, A. Vaziri, and A. Boudaoud. Wrinkling of pressurized elastic shells. *Phys. Rev. Lett.*, 107:174301, 2011.